

Entrapped Air in High-velocity Free-surface Flows on a Flat-sloped Spillway

S. Felder and A. Severi

Water Research Laboratory, School of Civil and Environmental Engineering,
UNSW Australia, Sydney, New South Wales, 2052, Australia

Abstract

An experimental study of high-velocity free-surface flows was conducted on a flat-sloped uncontrolled spillway with smooth bed providing novel insights into the entrapped air on spillways. In the present study the flow remained non-aerated despite reaching fully developed flow conditions as confirmed by boundary layer properties. The flow was characterised by strong free-surface fluctuation and instabilities downstream of the inception point of free-surface roughness. Phase-detection probes were employed to study the flow properties of entrapped air within the free-surface roughness region. The present study revealed strong interactions between air and water interfaces within this part of the flow providing useful information for air-water mass transfer processes in high-velocity free-surface flows.

Introduction

Spillways are commonly used to transfer waters safely and efficiently to lower elevations. They are classified based upon geometrical parameters such as slope, length and spillway roughness ranging from smooth invert to macro-roughness elements. Spillways are often associated with air entrainment commonly attributed to turbulent velocity fluctuations close to the free-surface. At the upstream end of a spillway, a turbulent boundary layer starts to develop and the flow is non-aerated and smooth. When velocity fluctuations close to the free-surface are strong enough to overcome both surface tension and buoyancy forces the air entrainment process starts at the inception point of free-surface aeration and downstream the flow is constantly aerated [4,14].

Experimental data suggest that this theory may not be the only mechanism contributing to the onset of free-surface aeration since air entrainment has been reported upstream of the intersection of boundary layer and free-surface [1,3]. Several researchers reported also of free-surface roughness upstream of the air-water flow region [1,5,12] which appears to be linked to small amplitude free-surface waves. When these waves start to collapse, the free-surface becomes rough and unstable at the inception point of free-surface roughness. While the free-surface roughness phenomenon has been reported previously, little information is available about the flow properties within this flow region for high-velocity free-surface flows.

Extensive research has been conducted on spillways with smooth bed and with steep slopes ($\theta > 30^\circ$) providing information about non-aerated and aerated flow properties along the spillway chute [3,8,11,14]. However limited research has been conducted of the non-aerated flow region on flat-sloped spillways ($\theta < 15^\circ$) despite some studies focusing on air-water flow properties downstream of the inception point of air entrainment [1,5,10].

Herein the present study investigated the flow patterns and properties on a flat-sloped spillway with smooth bed. For the investigated flow conditions, no free-surface aeration was observed despite reaching fully developed flow conditions before the downstream end of the spillway. Instead the experiments

revealed free-surface roughness and a layer of entrapped air at the air-water interface. Detailed measurements of the flow properties were conducted providing novel insights into entrapped air in high-velocity free-surface flows.

Experimental Facility and Instrumentation

Experiments were conducted in a large size spillway facility at UNSW's Water Research Laboratory (WRL). The spillway was uncontrolled and had a rectangular cross section of width $W = 0.8$ m, length $L = 9$ m, and slope $\theta = 11^\circ$. The spillway's side walls and channel bed were made of transparent Perspex with an estimated equivalent sand roughness of $k_s = 0.1$ mm (Fig. 1). Any joints in Perspex were thoroughly sealed to minimise any flow distortions and separations providing a smooth spillway chute. At the upstream end a header tank with honeycomb screens allowed for calm inflows into the spillway section via an uncontrolled crest with upstream rounded corner. Water was supplied from Manly Dam to the header tank providing constant flow rates monitored by a Venturi flow meter in the supply line.

Measurements of non-aerated flows were conducted with a Prandtl-Pitot tube with a diameter of $\varnothing = 3$ mm which was connected to an inclined 30° water manometer. The Pitot tube was mounted on a digital height gauge system which allowed placement of the Pitot tube within 1 mm accuracy. The Pitot tube was used to measure the time-averaged velocity distributions of non-aerated flows V_p in channel center line and at various cross-sections along the flume. The velocity data were also used for the estimation of the boundary layer development along the spillway.

In flow regions characterised by entrapped air, the Prandtl-Pitot tube was not able to measure the flow velocities accurately due to free-surface perturbations, entrapped air and fast fluctuations of the free-surface. In these flow regions, a dual-tip phase-detection intrusive probe was used instead to provide information about the flow properties of entrapped air at the air-water interface. The double-tip conductivity probe consisted of identical leading and trailing tips with inner electrode of $\varnothing = 0.125$ mm and transverse and longitudinal tip distances of $\Delta z = 1.1$ mm and $\Delta x = 4.85$ mm, respectively. Both conductivity probe sensors were sampled simultaneously for 45 s and with 20 kHz as recommended by [6]. The conductivity probe was excited by an electronic system designed at WRL and raw Voltage data were acquired with a high-speed data acquisition system NI USB-9162. The probe positioning in the flow direction was done with a specifically designed trolley system. The vertical profiling of flow properties was automated with an ISEL[®] robotic arm controlled by a single axis step controller IT 116 Flash with ± 0.01 mm accuracy. The data were collected with self-developed LabVIEW data acquisition software. At each cross-section, conductivity probe measurements were conducted at minimum 30 positions in a cross-section to allow a high-resolution recording of the flow properties in the flow region with entrapped air.

The raw Voltage signals of the conductivity probe were post-processed using data processing methods typically employed to air-water flows. In the present study, no air entrainment was

observed and typical air-water analysis techniques were applied to characterise the flow properties in the thin layer of entrapped air at the air-water interface. The Voltage signals of the leading probe tip were post processed based upon a single-threshold of 50% between air and water Voltages. The raw Voltage signal was decomposed into the instantaneous void fraction c indicating a water phase when the Voltage signal exceeded the single threshold value and air when the Voltage was below the threshold value. The integration of the instantaneous void fraction provided the time averaged local void fraction C and the number of changes of the air-to-water (and water-to-air) interfaces per unit time yielded the interface count rate F . Cross-correlation analyses of the leading and trailing tip signals provided the average travel time between the two probe sensors and the time-averaged interfacial velocity V_{CP} was calculated.

Along the spillway chute, the flow depths were measured with a pointer gauge. In the flow region with entrapped air, the free-surface was rough and fluctuated reducing the accuracy of flow depth measurement significantly. A Mikrotrotron™ MC4082 high-speed camera was used to record high-quality videos of the entrapped air. The frame rate was 457 Hz and the resolution of camera images was 2336×1728 pixel. All experiments and flow patterns were documented with a camera Canon™ EOS 1000D.

The experiments were conducted for a range of flow conditions (Table 1). Table 1 summarises the flow conditions including the discharge per unit width q_w , the critical flow depth d_c and the Reynolds number Re defined in terms of the hydraulic diameter. The Froude number varied along the spillway for all flow conditions between $1.7 < Fr < 10.5$. Table 1 lists also observations of characteristic lengths in the present study including the length from the upstream crest to the inception point of free-surface roughness (L_{FR}) and from the crest to the position where the flow was fully developed (L_{BL}).

q_w [m ² /s]	d_c [m]	Re [-]	L_{FR} [m]	L_{BL} [m]
0.019	0.0330	7.32×10^4	1.7	1.76
0.031	0.0464	1.21×10^5	2.3	2.51
0.050	0.0634	1.90×10^5	2.7	2.85
0.075	0.0831	2.81×10^5	3.0	3.98
0.100	0.1007	3.68×10^5	3.5	4.81
0.125	0.1168	4.54×10^5	3.7	5.60

Table 1. Experimental flow conditions in the present study; Summary of basic observations of characteristic lengths L_{FR} and L_{BL} .

Flow Patterns on the Flat-sloped Spillway

Detailed visual observations were conducted for the full range of flow conditions (Table 1). At the upstream end of the spillway, the flow accelerated and the flow depth decreased rapidly. Further downstream the flow depth declined gradually in streamwise direction approaching uniform flow conditions towards the downstream end of the spillway. While the flow surface was smooth and clear at the upstream end of the spillway, the free-surface became rough and unstable at some distance downstream from the spillway crest L_{FR} . This location was named as inception point of free-surface roughness L_{FR} (Fig. 1). Table 1 summarises the positions of L_{FR} for the present data highlighting an increase in L_{FR} with increasing discharge. Downstream of the inception point of free-surface roughness, the free-surface was fluctuating very fast and the fluctuations increased with increasing flow rate confirming observations by [9]. Figure 1A illustrates the inception point of free-surface roughness in the present study showing a change in free-surface patterns between the upstream flow region and the flow region downstream of L_{FR} . From the inception point of free-surface roughness to the end of the spillway, the flow surface was rough and some air was continuously entrapped in a small layer at the air-water interface (Fig. 1). Figure 1B shows a detail of the rough

free-surface from top view highlighting the fragmentation of the flow (Note that the white colour in Figure 1B was not associated with air entrainment, but with the flume support underneath the Perspex flume.) For all flow conditions, no air entrainment was observed and the flow did not show a whitish colour typically associated with air-water flows.



(A) Inception point of free-surface roughness (B) Top view of free-surface roughness

Figure 1. Observations of free-surface roughness in the present study; $q_w = 0.05$ m²/s, $d_c = 0.063$ m, $Re = 1.9 \times 10^5$, $L_{FR} = 2.7$ m

Due to the high-velocity of the flow and the fast fluctuations of the free-surface, the employment of the high-speed camera was required for more detailed visual observations of the free-surface roughness. Detailed high-speed videos were recorded in a flow region towards the downstream end of the spillway ($6.5 \leq x \leq 6.7$ m), where the flow was fully developed for all flow conditions (Fig. 2). Figure 2 illustrates typical images extracted from one of the side-looking high-speed videos with a time step of 10 ms between the two images. The photos show the flow features in 2 dimensions next to the side-wall of the spillway. The flow could be separated into three flow regions comprising a clear water flow region closest to the chute bed, an entrapped air region and a region of air above the flow. The clear water flow region was maintained throughout the spillway for all flow conditions and no air bubbles were observed indicating that the flow was non-aerated. For $q_w \geq 0.075$ m²/s, occasionally free-surface instability in the entrapped air region would release a single bubble into the upper area of the clear water flow region. The detachment of these bubbles appeared to be caused by Helmholtz instabilities within the entrapped air region. This process could be observed with the high-speed camera. The single air bubbles were advected downstream and sometimes broken up into smaller bubbles by turbulence. Interestingly, the bubbles did not rise immediately to the surface, but travelled just below the entrapped air region downstream. It appeared that turbulence forces at the interlayer between clear water and entrapped flow region were stronger than the buoyancy of air bubbles.

The entrapped air region was characterised by strong instability, free-surface roughness and free-surface fluctuations (Fig. 2). Figure 2 illustrates the flow from the site and the streaks in the entrapped flow region are a feature of both the fluctuations of the free-surface and of the entrapped flow region. Note that Fig. 2 shows only the flow features at the side-wall and not across the flume. The two images in Figure 2 are separated by a small time step revealing rapid changes at the air-water interface. Detailed measurements of the properties within this flow region were conducted with the phase-detection intrusive probe. Above the entrapped air region, a clear air region was observed reflecting the free-surface boundary above the flow (dark colour in Fig. 2). Note that no water droplets were ejected above the flows for all flow conditions.

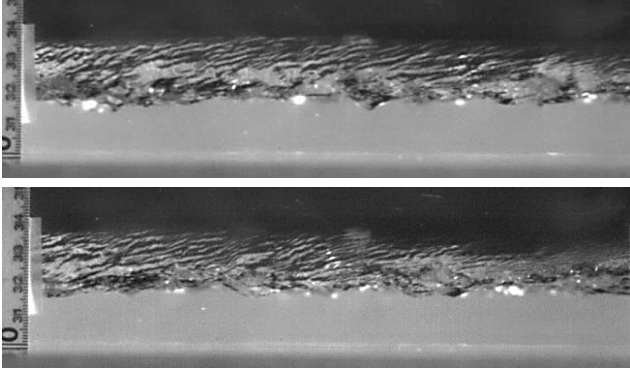


Figure 2. Free-surface roughness in fully developed flow region at $78.2 \leq x/d_c \leq 80.6$: $q_w = 0.075 \text{ m}^2/\text{s}$, $d_c = 0.083 \text{ m}$, $Re = 2.8 \times 10^3$, $L_{FR} = 3 \text{ m}$; Time step between photos: 10 ms (Flow from right to left).

Velocity and Boundary Layer Development

Velocity measurements were conducted with the Prandtl-Pitot tube at 16 positions between $0.42 \leq x \leq 8.76 \text{ m}$ for all flow conditions. In each cross-section, velocities were measured between the channel bed and as close as possible to the free-surface. The velocities increased along the spillway reaching uniform values towards the downstream end for all flow conditions in the present study.

At the spillway crest a turbulent boundary layer developed and increased in downstream direction. The velocities were analysed to identify the boundary layer thickness δ and the growth rate of the boundary layer along the flume. The boundary layer thickness was deduced from the experimental velocity data at the position where $V_p = 0.99 \times V_o$, where V_o is the free-stream velocity. Due to the limitations in velocity measurements very close to the free-surface, the graphical approach from [2] assisted to identify the intersection of the boundary layer with the free-surface. The lengths from the upstream end to the intersection point L_{BL} were recorded and are listed in Table 1. With increasing discharge, L_{BL} increased. The intersection of the boundary layer with the free-surface occurred consistently downstream of the inception point of free-surface roughness (Table 1) indicating that the free-surface roughness was not triggered by turbulence fluctuations within the water alone, but also by instabilities at the interface between air and water. Downstream of the L_{BL} , the flow became fully developed but no differences in free-surface roughness were observed. The boundary layer growth rate for the present experiments was estimated as:

$$\frac{\delta}{x} = 0.0235 \times \left(\frac{x}{k_s} \right)^{-0.135} \quad (1)$$

The boundary layer growth was in good agreement with previous experiments on spillways with smooth inverts [2,14]. For all flow conditions, the velocity data were best correlated with a power law within the turbulent boundary layer:

$$\frac{V_p}{V_o} = \left(\frac{y}{\delta} \right)^{\frac{1}{6.4}} \quad (2)$$

In Figure 3, all velocity data of the present study are compared with the best fit correlation (Eq. 2) revealing a very close correlation with the power law. The present 1/6.4th power law was close to observations by [4] on a flat-sloped spillway ($\theta = 4^\circ$).

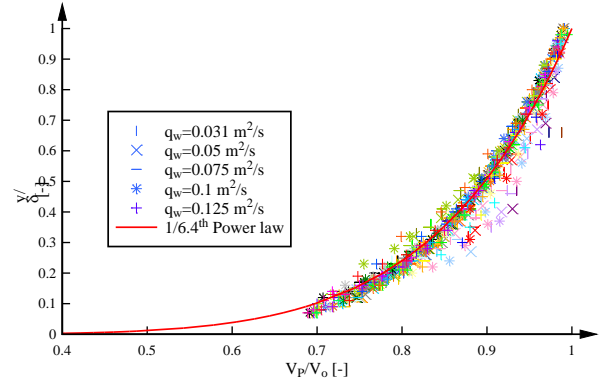


Figure 3. Dimensionless time averaged velocity distributions along the spillway ($\theta = 11^\circ$); Comparison with power law (Eq. 2) for all flow conditions (Table 1).

Entrapped Air Properties at the Air-water Interface

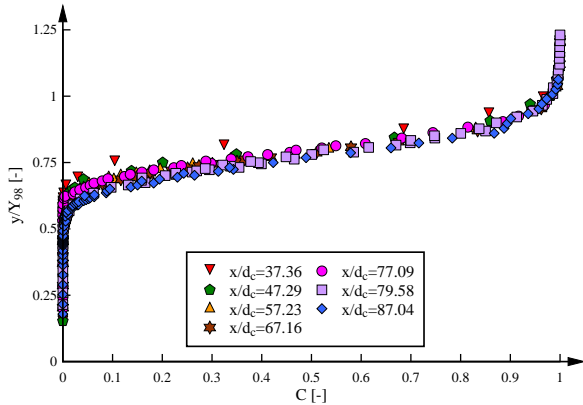
Detailed measurements of the flow properties within the entrapped air region were performed with the double-tip conductivity probe at several locations downstream of the inception point of free-surface roughness. Basic results are presented in Figure 4 in dimensionless terms including the void fraction C (Fig. 4A), the air-water interface count rate $F \times d_c/V_c$ (Fig. 4B) and the interfacial velocity V_{Cp}/V_{98} , where V_{98} is the characteristic velocity where $C = 0.98$ (Fig. 4C). The distributions are shown as a function of dimensionless distance above channel invert y/Y_{98} , where Y_{98} is the distance where $C = 0.98$. In a detailed sensitivity analysis, the characteristic depth Y_{98} was selected as the depth where the variability in flow depth was the smallest following the approach by [13].

Typical void fraction distributions are shown in Fig. 4A for several cross-sections downstream of the inception point of free-surface roughness. The void fraction distributions exhibited typical S-shapes and a close agreement for all measured positions. In the non-aerated flow region underneath the entrapped air region ($y/Y_{98} < 0.6$), almost no void fraction was detected and in the air flow region above the entrapped air region ($y/Y_{98} > 1.05$) the void fraction was $C \approx 1$. The depth-averaged mean void fraction C_{mean} was calculated in each cross-section using Y_{98} as upper boundary. For all data, the mean void fraction increased gradually along the spillway from $C_{mean} = 0.17$ just downstream of the inception point of free-surface roughness to $C_{mean} = 0.28$ at the downstream end of the spillway. Note that C_{mean} did not reach uniform conditions. The increase of C_{mean} in flow direction is also visible in Figure 4A in a small downwards shift of the void fraction distributions in flow direction.

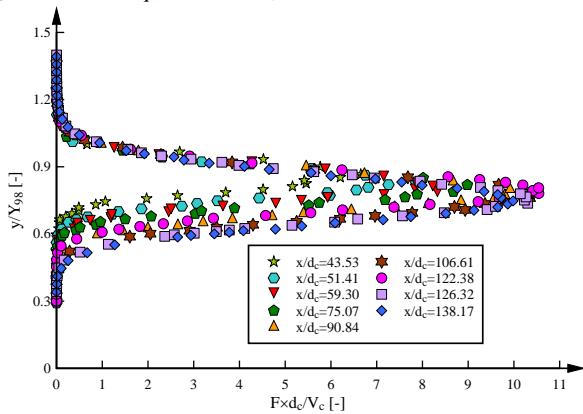
Distributions of air-water interface count rate are illustrated in Figure 4B for one flow rate indicating a significant number of changes between air and water interfaces within the entrapped air region. The number of air-water interfaces was largest for $C \approx 0.5$ and decreased towards very small values for $y/Y_{98} < 0.55$ and $y/Y_{98} > 1.05$ respectively (Fig. 4B). Downstream of the inception point of free-surface roughness, the number of interfaces increased rapidly to reach almost constant distributions of F towards the downstream end of the spillway (Fig. 4B). The finding of significant void fractions and interfacial count rates within the entrapped air region is an indicator for significant air-water interactions within this part of the flow which may be associated with air-water mass transfer processes [7].

Figure 4C presents the dimensionless interfacial velocity distributions V_{Cp}/V_{98} for all flow conditions in the present study. The velocities are compared with the 1/6.4th power law derived from the Pitot tube measurements (Eq. 2). Despite some data scatter, the conductivity observations showed a relatively close

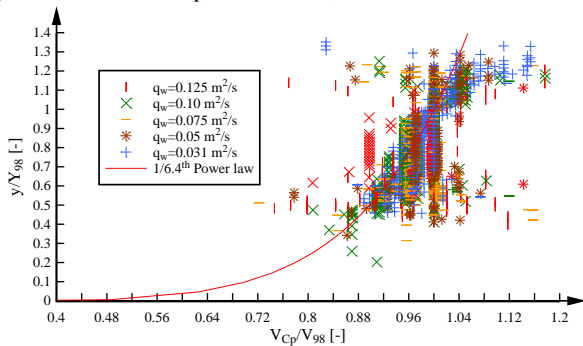
agreement for $0.6 < y/Y_{98} < 1.05$ (Fig. 4C). The strongest data scatter and potentially suspicious velocities were observed for $y/Y_{98} < 0.6$ and for $y/Y_{98} > 1.05$ respectively due to the small number of air-water interfaces within these parts of the flow (Fig. 4B). The time-averaged velocities recorded with the Pitot tube and the conductivity probe V_P and V_{Cp} respectively were in good agreement at all positions along the spillway confirming that a double-tip conductivity probe is suitable for the measurement of average flow velocities within entrapped air flows if the interface count rate is sufficiently large.



(A) Void fraction: $q_w = 0.1 \text{ m}^2/\text{s}$, $d_c = 0.101 \text{ m}$, $Re = 3.7 \times 10^5$.



(B) Interface count rate: $q_w = 0.05 \text{ m}^2/\text{s}$, $d_c = 0.063 \text{ m}$, $Re = 1.9 \times 10^5$.



(C) Comparison of dimensionless interfacial velocity distributions with power law (Eq. (2)) for all flow conditions in the present study.

Figure 4. Distributions of entrapped air properties downstream of the inception point of free-surface roughness.

Conclusion

An experimental study was conducted on an uncontrolled flat-sloped spillway ($\theta = 11^\circ$) with smooth bed for a range of flow conditions. Observations of the flow patterns revealed strong free-surface roughness which appeared to be caused by collapse of small amplitude waves at the free-surface and not by the interaction of turbulent boundary and free-surface. Despite reaching fully developed flow conditions, no air entrainment was

observed in the present study. Instead, detailed observations of the entrapped air properties provided new insights into the free-surface roughness. Systematic measurements of entrapped air properties were conducted using phase-detection intrusive probes providing distributions of void fraction, air-water interface count rate and interfacial velocity within a small layer at the air-water interface. The data revealed strong air-water interactions within the entrapped air region within a narrow band $0.6 < y/Y_{98} < 1.05$. The flow properties showed distributions similar to fully aerated air-water flows and a slight increase of characteristic properties along the spillway. The observations provided novel insights into the air-water interface in high-velocity flows which may be useful for a better understanding of air-water mass transfer processes.

References

- [1] Anwar, H., Discussion of Self-aerated flows on chutes and spillways by Chanson, H., *J. Hydraulic Eng. (ASCE)*, **120**, 1994, 778-779.
- [2] Bauer, W.J., Turbulent boundary layer on steep slopes, *Trans. Am. Soc. Civil Eng.*, **119**, 1954, 1212-1233.
- [3] Cain, P. Measurements within self-aerated flow on a large spillway, *PhD thesis*, School of Civil Engineering, University of Canterbury, New Zealand, 1978.
- [4] Chanson, H., Air bubble entrainment in open channels: flow structure and bubble size distributions, *Int. J. Multiphase Flow*, **23**, 1997, 193-203.
- [5] Chanson, H., Closure to "Self-Aerated Flows on Chutes and Spillways" by Chanson, H., (February, 1993, Vol. 119, No. 2). *J. Hydraulic Eng.*, **120**, 1994, 779-782.
- [6] Felder, S. & Chanson, H., Phase-detection probe measurements in high-velocity free-surface flows including a discussion of key sampling parameters, *Exp. Therm. Fluid Sci.*, 2015, **61**, 66-78.
- [7] Felder, S. & Chanson, H., Aeration and air-water mass transfer on stepped chutes with embankment dam slopes, *Environmental Fluid Mechanics*, **15**, 2015, 695-710.
- [8] Killen, J.M., The surface characteristics of self-aerated flow in steep channels, *PhD thesis*, University of Minnesota, Minneapolis, USA, 1968.
- [9] Koloseus, H.J., & Davidian, J., Free-surface instability correlations and Roughness-concentration effects on flow over hydrodynamically rough surfaces, *U.S. Geol. Surv. Water Supply Pa.*, 1592-D, 1966.
- [10] Lai, K.K., A study of air entrainment in steep open channels, *Third Australasian Conference on Hydraulics and Fluid Mechanics*, Sydney, Australia, 1968, 41-44.
- [11] Straub, L.G., & Anderson, A.G., Experiments on self-aerated flow in open channels. *J. Hydraulic Div. (ASCE)*, **84**, 1958, 1-35.
- [12] Valero, D. & Bung, D.B., Development of the interfacial air layer in the non-aerated region of high-velocity spillway flows, *Int. J. Multiphase Flow*, **84**, 2016, 66-74.
- [13] Wilhelms, S.C. & Gulliver, J.S., Bubbles and waves description of self-aerated spillway, *J. Hydraul. Res.*, **43**, 2005, 522-531.
- [14] Wood, I.R., Ackers, P. & Loveless, J., General method for critical point on spillways, *J. Hydraulic Eng. (ASCE)*, **109**, 1983, 308-312.